Journal of ELECTRONIC MATERIALS, Vol. 50, No. 3, 2021
https://doi.org/10.1007/s11664-020-08687-6
© 2021 The Minerals, Metals & Materials Society

ORIGINAL RESEARCH ARTICLE

MoS_2 Thin Films Grown by Sulfurization of DC Sputtered Mo Thin Films on Si/SiO_2 and C-Plane Sapphire Substrates

N. AKCAY,[1,2,5] M. TIVANOV,[3] and S. OZCELIK[1,4,6]

1.—Photonics Application and Research Center, Gazi University, 06500 Ankara, Turkey. 2.—Department of Mechanical Engineering, Faculty of Engineering, Baskent University, 06790 Ankara, Turkey. 3.—Faculty of Physics, Belarusian State University, 220030 Minsk, Belarus. 4.—Department of Photonics, Faculty of Applied Sciences, Gazi University, 06500 Ankara, Turkey. 5.—e-mail: akcayneslihan@yahoo.com. 6.—e-mail: sozcelik@gazi.edu.tr

Here we report the growth of molybdenum disulfide (MoS_2) films with different thicknesses on silicon dioxide/silicon (SiO_2/Si) and c-plane sapphire substrates by sulfurization of direct current (DC) sputtered Mo precursor films in a chemical vapor deposition furnace with sulfur powder at 900°C. The structural, morphological, optical, and electrical properties of the films on different substrates were investigated through a series of characterization in detail. X-ray diffraction (XRD) results showed that the grown films on sapphire substrates had better crystallization and a well-stacked layered structure than the films on SiO_2/Si substrates. The frequency difference between the characteristic modes E^1_{2g} and A_{1g} of hexagonal phase MoS_2 was determined as $\sim 26\ cm^{-1}$ which is consistent with the typical value of bulk MoS_2. Energy-dispersive x-ray (EDX) spectra exhibited that the films were near-stoichiometric. A small shift towards the lower binding energies in the Mo $3d_{5/2}$ peak positions was observed due to the valency of Mo below +4 depending on the compositional ratios of the films in x-ray photoelectron spectroscopy (XPS) spectra. Atomic force microscopy (AFM) and scanning electron microscopy (SEM) analysis indicated that the films had smooth surfaces and a well-packed crystal structure. However, when the thickness of the films deposited on sapphire substrates increased, the strain between the sapphire substrate and MoS_2 film caused the formation of the micro-domes in the film. In addition, the films exhibited high absorption and reflection properties in the near-infrared (NIR) and mid-infrared (MIR) regions in Fourier transform infrared (FTIR) analysis. Therefore, it is considered that the films can be used for photodetector applications in these regions and infrared shielding coating applications.

Key words: Transition metal dichalcogenides, MoS_2 films, molybdenum disulfide, sulfurization, CVD, FTIR

INTRODUCTION

Molybdenum disulfide (MoS_2), which is a member of transition metal dichalcogenides (TMDCs; MX_2, where M = molybdenum (Mo) or W and X = sulfur (S) or selenium (Se)) family, has recently gained great attention due to its unique electrical, mechanical, optical and magnetic properties.[1–5] It is a semiconductor material that has a layered structur,e and while the atoms within each layer in MoS_2 are strongly covalently bonded, the adjacent layers are held together by weak van der Waals interactions.[6,7] These weak van der Waals interactions enable exfoliation of MoS_2 to individual atomically thin layers.[8] Single and multilayer thin films of MoS_2 have interesting properties such as thickness-

(Received October 7, 2020; accepted December 8, 2020; published online January 8, 2021)

dependent band gap,[9] high carrier mobility,[10] large surface-to-volume-ratio,[11] strong spin-valley coupling,[12] chemical stability, and high mechanical flexibility.[13,14] The monolayer of MoS_2 shows a direct energy band gap ($\sim$ 1.9 eV), whereas the multilayer/bulk of MoS_2 shows an indirect band gap ($\sim$ 1.3 eV).[15] These properties make MoS_2 a promising material in future nanoscale electronic and optoelectronic device applications such as photocatalysis,[16] photodetectors,[17] biosensors,[18] gas sensors,[19] phototransistors,[20] field-effect transistors (FETs),[21] solar cells [22] and light-emitting diodes (LEDs).[23]

There have been many various attempts including top-down and bottom-up methods such as mechanical exfoliation,[24] chemical exfoliation,[25] hydrothermal synthesis,[26] physical vapor deposition (PVD),[27] and chemical vapor deposition (CVD) [28] to produce MoS_2 thin films. Initially, researchers have intensely focused on the exfoliation method for obtaining monolayers of MoS_2 films and it is still the most commonly used method for the growth of MoS_2 films. However, it has been recently thought that the exfoliation method is not suitable for their large-scale production[29,30] because exfoliation results in the formation of MoS_2 flakes with random thicknesses at random distributions.[31,32] Therefore, they are considered to be limited in terms of controlling the thickness and thus the number of MoS_2 layers. In this context, the synthesis of uniform large-area MoS_2 layers by controlling the film thickness is necessary for the practical use of this material in electronic and optoelectronic applications in the industry. CVD is one of the most promising methods to produce continuous MoS_2 films over large areas as an alternative to exfoliation methods. Another advantage of CVD is that it can be avoided from the interfacial contamination during the layer by layer transfer process.[6,33,34] Various approaches such as high-temperature sulfurization of sputtered Mo films [35] or molybdenum trioxide (MoO_3),[28] molybdenum pentachloride ($MoCl_5$),[36] thermolysis of ammonium tetrathiomolybdate ($(NH_4)_2MoS_4$) [37] and chemical reaction of molybdenum hexacarbonyl ($Mo(CO)_6$) and diethyl sulfide ($(C_2H_5)_2S$) [38] can be used for the synthesis of MoS_2 films by using CVD. However, the controllable growth of MoS_2 films over large areas by CVD is still a big challenge and there are shortcomings in the fundamental understanding of the CVD growth process. For this reason, the optimization studies on the growth of MoS_2 films by CVD are still underway.

Our previous study has presented the production of MoS_2 films from direct current (DC)-sputtered Mo films using a two-zoned CVD system.[39] In this process, S powder and Mo films were placed in different zones having different temperature values. The films produced with this method had a highly oriented polycrystalline structure on silicon dioxide/silicon (SiO_2/Si) and sapphire substrates, but they were non-stoichiometric. Therefore, the carrier mobility values of the films were relatively low. To improve the film characteristics, in this study, a one-zoned CVD system was utilized to produce MoS_2 thin films on SiO_2/Si and sapphire substrates. In this context, structural, morphological, optical, and electrical characteristics of the grown films were reported in detail as a function of thickness. To comprehensively identify the structural and morphological properties and determine S/Mo ratios of the MoS_2 thin films with different thicknesses, the films were characterized by x-ray diffraction (XRD), Raman spectroscopy, secondary ion mass spectroscopy (SIMS), atomic force microscopy (AFM), scanning electron microscopy (SEM), energy dispersive x-ray (EDX), and x-ray photoelectron spectroscopy (XPS). The optical properties of the films were presented in both ultraviolet–visible (UV–Vis) and infrared (IR) regions. In addition, their electron-transport properties were investigated by room temperature Hall effect measurements. We believe that the growth of the MoS_2 films by this approach will provide an opportunity for the growth of large-area single and multilayer films of MoS_2. Therefore, we aim to focus on reducing the thickness of the Mo precursor films depending on the deposition time and produce thinner MoS_2 films over large areas by this approach in future studies. Moreover, we consider that the characterization results of the films obtained by using a lot of different techniques in our study will contribute to the literature as important scientific outputs and the grown MoS_2 films in our study can be used for the development of near-infrared (NIR) and mid-infrared (MIR) electro-optical devices and IR shielding coating applications due to their high absorption and reflection properties in the NIR and MIR regions.

EXPERIMENTAL

MoS_2 films were prepared on SiO_2/Si and c-plane sapphire substrates by sulfurization of DC-sputtered Mo precursor films. Prior to the deposition process, the substrates were ultrasonically cleaned in acetone and ethanol for 5 min, respectively. Afterwards, they were blow-dried by a high-purity nitrogen jet. The deposition of the precursor films was conducted in a three-target co-sputtering system at room temperature. The schematic diagram of the co-sputtering system and the deposition process of Mo precursor films were given in Fig. 1.

A Mo target with a purity of 99.95% was used to deposit the Mo precursor films. After the base pressure of the sputtering system was reached to $\sim 1.33 \times 10^{-7}$ kPa, the deposition process was started at a working pressure of 6.67×10^{-4} kPa in argon (Ar) atmosphere for all deposition processes. The sputtering power was 60 W and the deposition times were determined as 12 min and 17 min to obtain the films with the different thicknesses both on SiO_2/Si and c-plane sapphire substrates. The

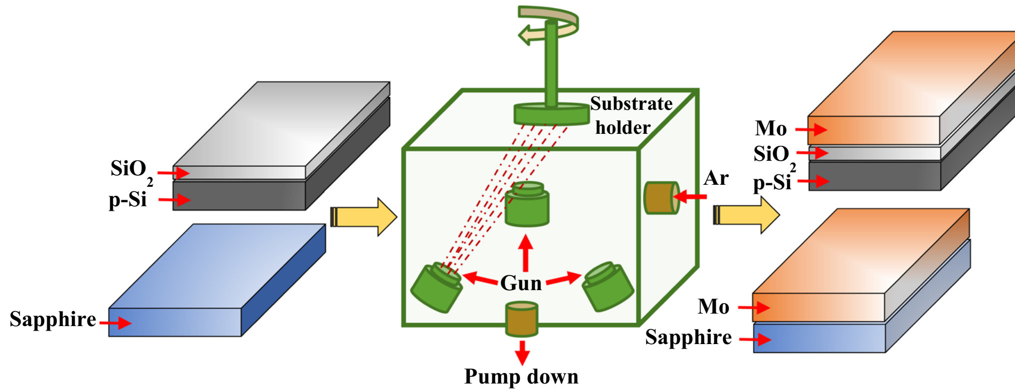

Fig. 1. The schematic diagram of the co-sputtering system and the deposition process of Mo precursor films.

Table I. The deposition times for the Mo precursor films on SiO_2/Si and sapphire substrates and the corresponding thickness values obtained by the profilometer measurement

Precursor films	Deposition time (min)	Thickness (nm)
On SiO_2/Si	12	95
	17	135
On sapphire	12	100
	17	132

deposition times for the precursor films and the corresponding thickness values obtained by profilometer measurement are presented in Table I.

All deposited Mo precursor films in this work were treated to the same sulfurization process. Figure 2 depicts the schematic diagram of the sulfurization furnace and temperature–time profile of the sulfurization process. Firstly, the precursor films and 0.5 g of elemental sulfur (S) powder (99.999%) were placed into a quartz boat which was loaded into the quartz tube furnace. The quartz tube furnace was pumped down to a base pressure of $\sim 10^{-3}$ mbar and flushed with Ar gas flow before the sulfurization process.

The precursor films were heated to 900°C at a ramping rate of ~ 20°C/min and maintained at this temperature for 90 min. The working pressure was kept at 3.4 mbar during the entire sulfurization process. Finally, the samples were cooled down to room temperature at a rate of 10°C/min. The sulfurized films of Mo precursors with the thicknesses of 95 nm, 135 nm, 100 nm, and 132 nm deposited on SiO_2/Si and c-plane sapphire substrates were named as Si1, Si2, Sa1, and Sa2 regarding the name of the substrates, respectively.

The crystal structure of MoS_2 films was analyzed by using an APD 2000 PRO x-ray diffractometer equipped with a Cu-Kα source (λ = 1.54052 Å). Raman scattering measurements were carried out by a Nanofinder HE (LOTIS TII) confocal Raman spectrometer at room temperature. For the excitation, a 532 nm continuous-wave solid-state laser was used. Raman spectra were obtained with a spectral resolution better than 3.0 cm^{-1}. The composition and the morphology of the films were investigated by a Hitachi S–4800 (Japan) scanning electron microscope arranged with an EDX spectrometer. The surface morphology of the films was also examined by AFM analysis by using a Solver Nano tool (NT-MDT) in the semi-contact mode with a scanning probe of 10 nm tip radius. XPS studies were performed by using an Omicron XPS setup with a Mg Kα x-ray source (1253.6 eV) operating at 10 kV. High-resolution scans were obtained at 20 eV. The peak positions were calibrated based on the C1s peak at 284.6 eV. The elemental depth profile of the films was acquired by SIMS using a Hiden Analytical SIMS Workstation. A primary beam of O^{2+} ions with an energy of 3.850 keV and a beam current of 400 nA were used for the analysis. UV–Vis spectroscopy (Perkin Elmer Lambda 2S) was used to collect the optical transmittance and reflectance spectra of the films. Fourier transform infrared (FTIR) spectra were obtained by Bruker Vertex 80 FTIR spectrometer in the spectral area between 400 cm^{-1} and 7500 cm^{-1} at room temperature. The number of scans was fixed to 32 with a spectral resolution of 4 cm^{-1}. The electrical properties of the films including carrier mobility, carrier density, and resistivity were characterized by the van der Pauw technique at room temperature using LakeShore Hall-effect measurement system. The thickness values of the Mo precursor films and the sputtering depths from SIMS craters were determined by a stylus type profilometer (Veeco, Dektak 150).

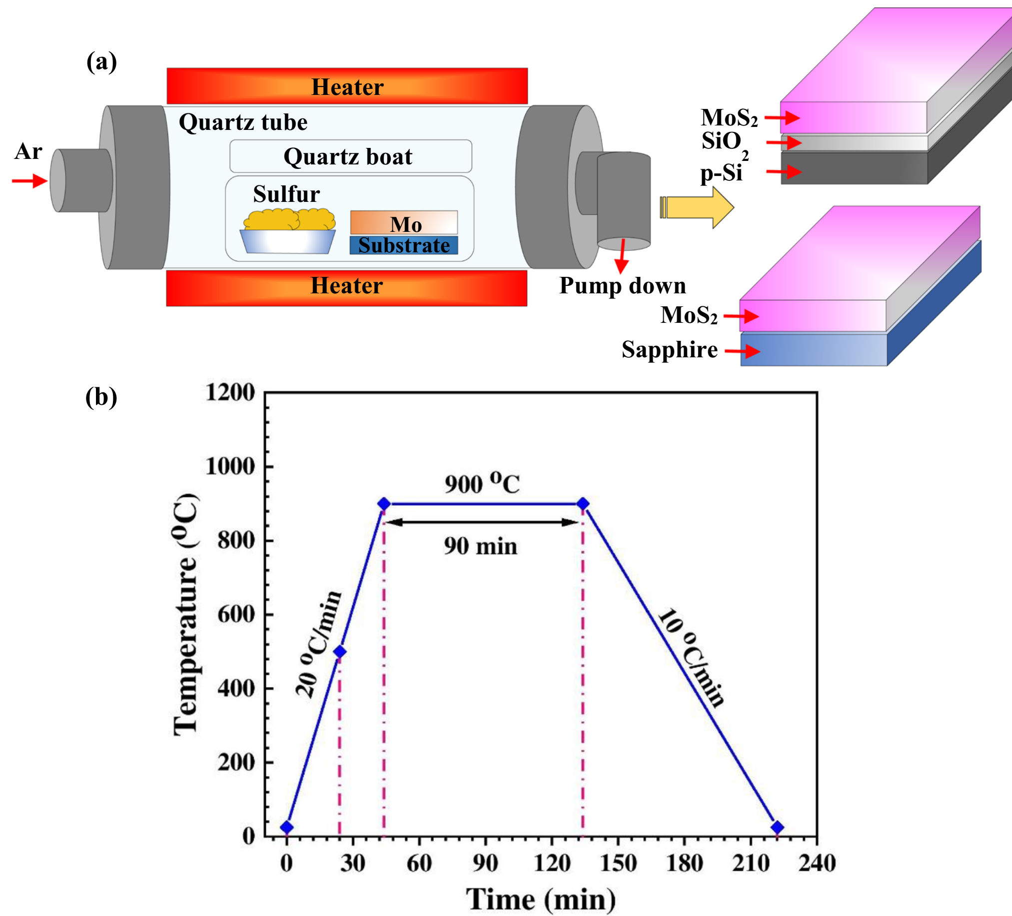

Fig. 2. (a) The schematic diagram of the sulfurization furnace and (b) the temperature–time profile of the sulfurization process of the Mo precursor films.

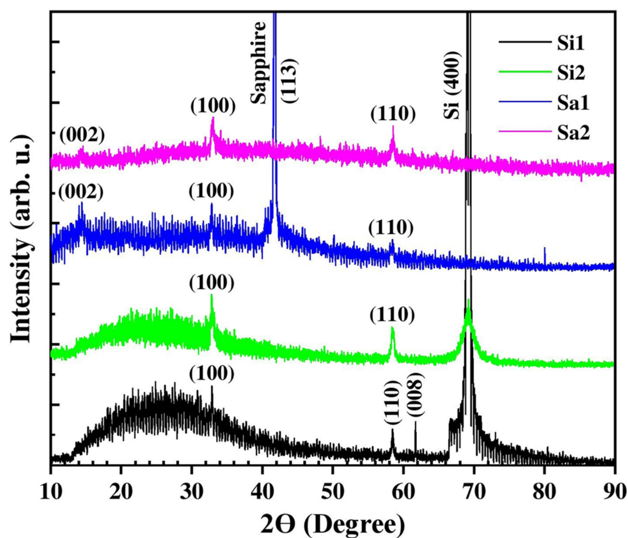

Fig. 3. XRD patterns of the MoS_2 films grown on SiO_2/Si and c-plane sapphire substrates at 900°C.

RESULTS AND DISCUSSION

The XRD patterns of MoS_2 thin films with different thicknesses prepared on SiO_2/Si and c-plane sapphire substrates are given in Fig. 3. All the films exhibited two diffraction peaks at $2\theta = 32.82°$ and $2\theta = 58.78°$ corresponding to (100) and (110) planes of hexagonal MoS_2, respectively (JPDS:37-1492).

For the sample Si1, another observed peak at $2\theta = 61.97°$ was attributed to the (008) plane of hexagonal MoS_2. The peaks corresponding to the (400) and (113) crystal planes of Si and c-plane sapphire coming from substrates appeared at $2\theta = 69.57°$ and $2\theta = 42.37°$ for the samples Si1, Si2, and Sa1, respectively. The diffraction peaks corresponding to the (002) crystal plane of hexagonal MoS_2 were obtained for the films grown on sapphire substrates. With the appearance of the (002) diffraction peak at $2\theta = 14.37°$ for the films grown on c-plane sapphire substrates, it can be concluded that the MoS_2 films on c-plane sapphire substrates had better crystallization and well-stacked layered structure than those of the films on SiO_2/Si substrates. As a result, the XRD patterns revealed that the grown films in this study were

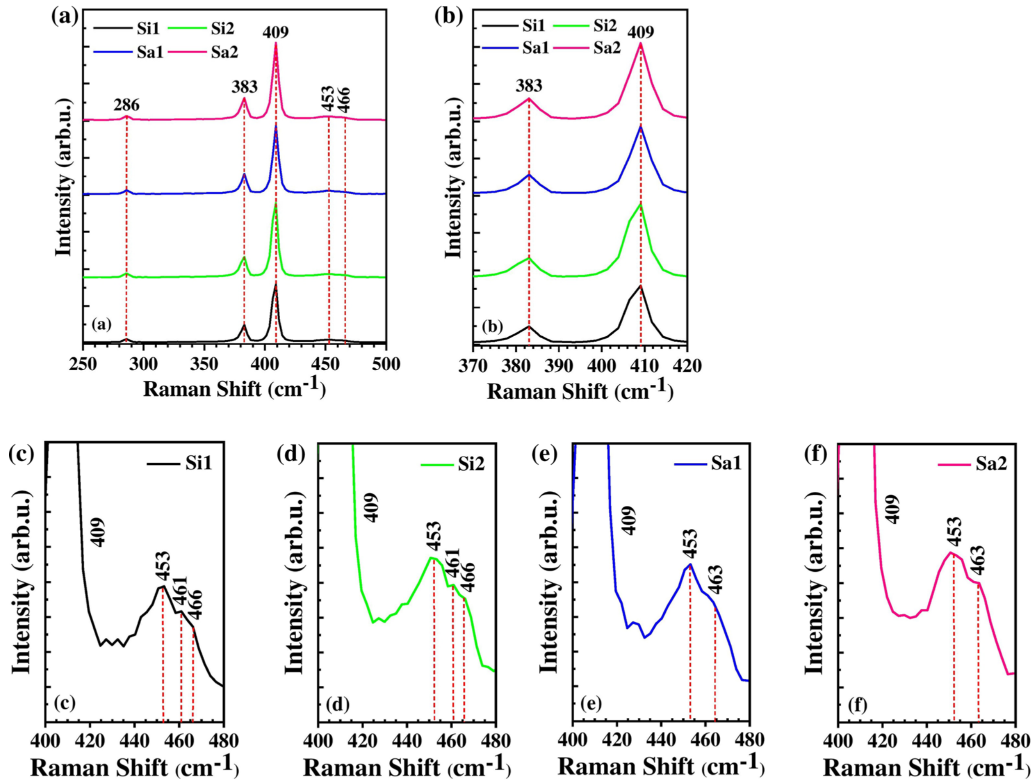

Fig. 4. (a) Raman spectra of the MoS_2 films. (b) The expanded Raman spectra of the MoS_2 films in the range of 370–420 cm^{-1}. The expanded Raman spectra of the samples (c) Si1, (d) Si2, (e) Sa1, and (f) Sa2 in the range of 400–480 cm^{-1}.

predominantly oriented along the c-axis which represents favorable crystal growth orientation of the hexagonal MoS_2.

Figure 4a shows the Raman spectra of MoS_2 films. The characteristic modes E^1_{2g} (in-plane vibration of Mo and S atoms) and A_{1g} (out-of-plane vibration of S atoms) of hexagonal phase MoS_2 were observed at around 383 cm^{-1} and 409 cm^{-1} with a difference of $\sim$ 26 cm^{-1} Raman shift (frequency difference, $\Delta = A_{1g} - E^1_{2g}$) which is consistent with the typical value of bulk MoS_2, respectively.[9,40]

The full width at half maximum (FWHM) values and the intensity of the characteristic peaks may give an impression about the crystal quality of the films.[37] The FWHM value for the sample Sa2 (7 cm^{-1}) was slightly higher than that of the others (6 cm^{-1}). This was attributed to a decrease in the crystallinity of the sample Sa2 due to the formation of micro-domes on the surface of the film, as will be discussed in AFM and SEM analysis later. On the other hand, the intensities of the peaks were higher for the films grown on the c-plane sapphire substrates than those of the films grown on SiO_2/Si substrates and increased with the increase in the thicknesses of the films. The expanded Raman spectra in the range of 370–420 cm^{-1} and 400–480 cm^{-1} are given in Fig. 4b, c, f, respectively. The small peaks of E_{1g}, 2LA(M), and A_{2u} modes were also detected at 286 cm^{-1}, 453 cm^{-1}, and 463/466 cm^{-1} in the spectra of the films.[3,35,40–42] The MoS_2 films with different thicknesses prepared on different substrates did not show remarkable differences in Raman peak positions.

The elemental composition of the films was analyzed by EDX. Figure 5 shows EDX spectra of the films with insets indicating of atomic percentage % and atomic ratios of S and Mo.

The S/Mo ratios of the samples Si1, Si2, Sa1, and Sa2 were determined as 2.30, 1.98, 1.92, and 1.90, respectively. These results showed that the composition value of the sample Si2 was the nearest to the stoichiometric value 2 obtained from the S/Mo ratio for the MoS_2 compound and by the increase in the thicknesses of the Mo precursor films, binding of S element to Mo element decreased during the sulfurization. It has been clearly seen that the increase in the chalcogen vapor pressure with the decrease in the volume of the sulfurization atmosphere thanks to the use of the single-zoned CVD furnace caused an increase in the incorporation of S atoms into the MoS_2 matrix. This caused the composition values to come much closer to the stoichiometric value 2 in this study. As seen in Fig. 5, for all samples, EDX spectra exhibited a peak corresponding to the platinum (Pt) element which is a consequence of the fact that the samples were sprayed with platinum before SEM and EDX analysis. Furthermore, the Si, aluminum (Al), and oxygen (O) signals coming from SiO_2/Si and sapphire (Al_2O_3) substrates were also detected in the spectra. Even

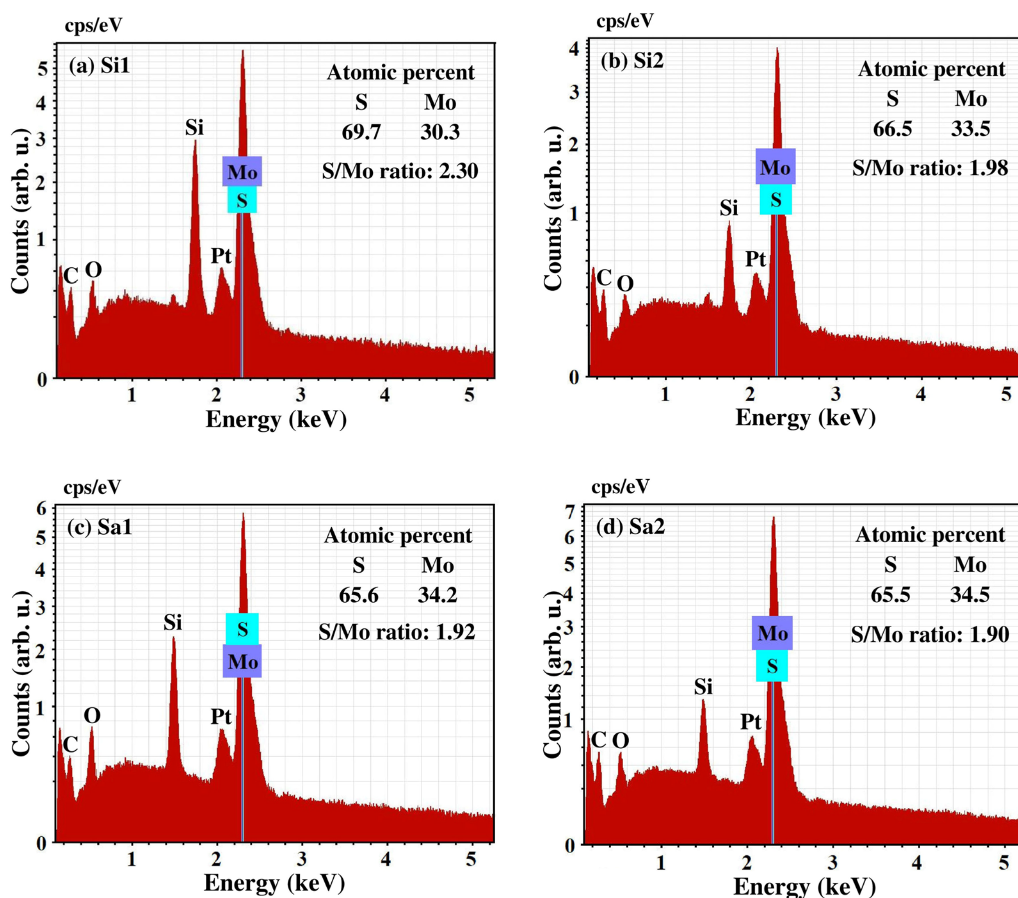

Fig. 5. EDX spectra of the samples (a) Si1, (b) Si2, (c) Sa1, and (d) Sa2.

though the Si, Al, Pt, carbon (C), and O signals originating from the substrates and contaminations in the films appeared in EDX spectra, the Mo and S signals were the strongest in the spectra.

XPS measurements were carried out to obtain information regarding the chemical states of the films. High-resolution XPS spectra for Mo 3d and S 2p core levels of the films grown on SiO_2/Si and sapphire substrates were shown in Fig. 6. The samples Si1 and Si2 exhibited Mo binding energies of 229.6 eV, 229.3 eV corresponding to Mo $3d_{5/2}$ and 232.4 eV, 232.1 eV corresponding to Mo $3d_{3/2}$ orbitals of Mo^{+4} states, respectively (Fig. 6a, b). In the case of the samples Sa1 and Sa2, it was seen that the characteristic peaks corresponding to the Mo $3d_{5/2}$ and Mo $3d_{3/2}$ doublet were located at $\sim$ 229.2 eV and $\sim$ 231.8 eV, respectively (Fig. 6c and d). The S binding energies for all samples were observed at around 161.8 eV and 163.6 eV corresponding to S $2p_{3/2}$ and S $2p_{1/2}$ orbitals of divalent sulfide ions (S^{2-}), respectively (Fig. 6e, f, g and h). In addition, a peak appeared at around 226 eV for all samples, which corresponds to S 2 s binding energy. The binding energy values of Mo 3d, S2s, and S2p states in the films were presented in Table II.

The XPS results showed that there was a small shift towards the lower binding energies in the Mo $3d_{5/2}$ peak positions depending on the compositional ratios of the films discussed in the EDX analysis above. This small shift was attributed to the valency of Mo below +4 due to the formation of the films in MoS_{2-x} structure in our study. Similar results related to the shift in Mo $3d_{5/2}$ peak positions were obtained by Zeng and et al. and Baker et al.[43,44] The linear relationship between the MoS_{2-x} stoichiometry and Mo $3d_{5/2}$ binding energy can be seen in Fig. 7.

Two-dimensional (2D) 10 $\times$ 10 μm^2 AFM images of the films are given in Fig. 8. Roughness parameters and average grain size values of the films obtained by AFM analysis are given in Table III. From the AFM images, it was observed that all the grown films had uniform surfaces except for the sample Sa2. The MoS_2 film of the sample Sa1 on the sapphire substrate was the smoothest one with a root mean square roughness (R_{rms}) value of 5.95 nm among the samples.

On the other hand, sample Sa2 exhibited the roughest morphology due to the micro-domes on its surface. Although the c-plane sapphire substrate has the same hexagonal symmetry as MoS_2, there is a large coefficient of thermal expansion mismatch between them.[45,46] This mismatch causes an increase in the strain between the sapphire

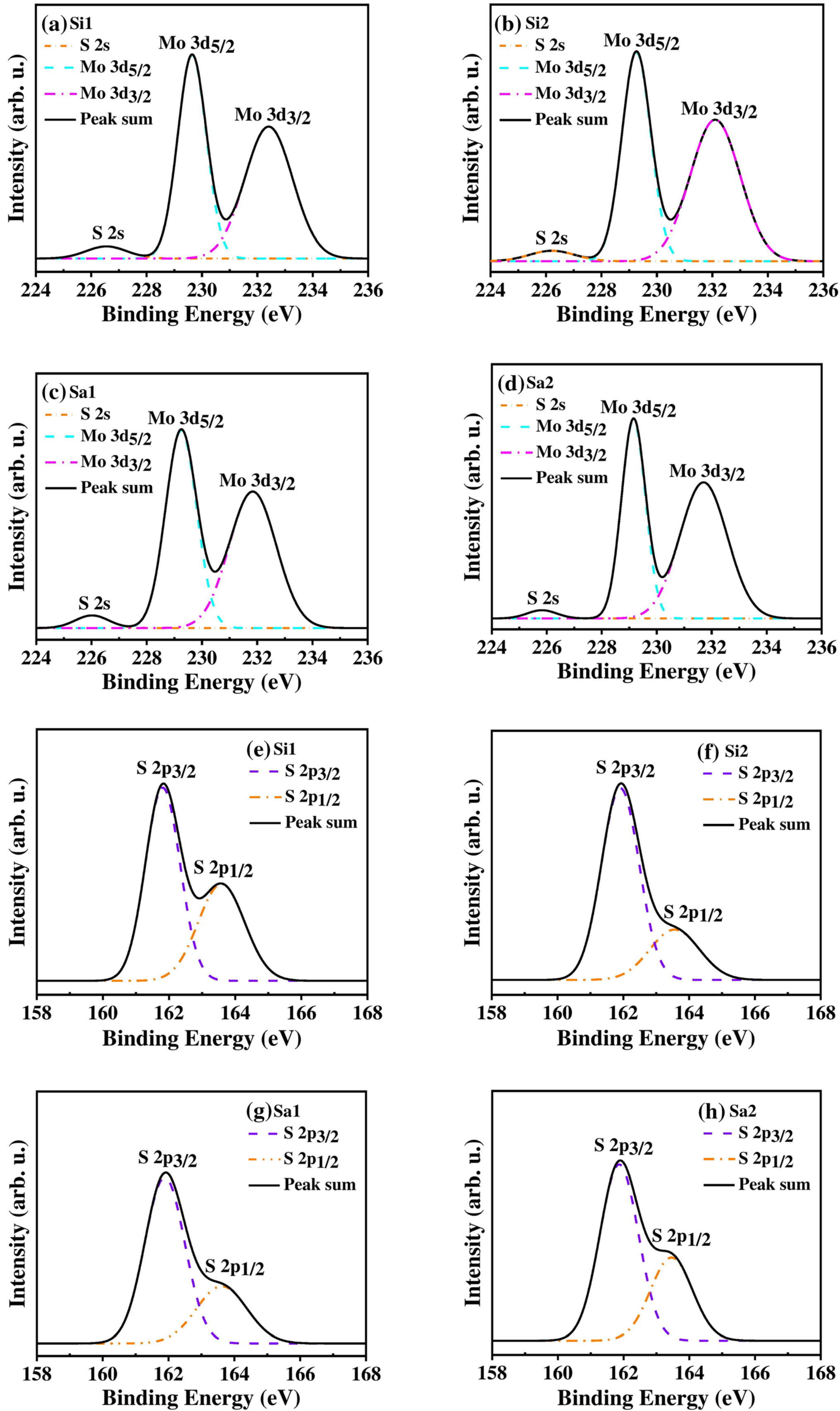

Fig. 6. High-resolution XPS spectra of the samples (a,e) Si1, (b,f) Si2, (c,g) Sa1, and (d,h) Sa2 for Mo 3d and S 2p core levels, respectively.

Table II. The binding energy values of Mo 3d, S2 s, and S2p states in the films

	Binding Energy (eV)				
Sample	**Mo $3d_{5/2}$**	**Mo $3d_{3/2}$**	**S 2s**	**S $2p_{3/2}$**	**S $2p_{1/2}$**
Si1	229.64	232.41	226.55	161.81	163.69
Si2	229.25	232.10	226.22	161.91	163.56
Sa1	229.24	231.84	226.02	161.89	163.62
Sa2	229.15	231.70	225.82	161.87	163.46

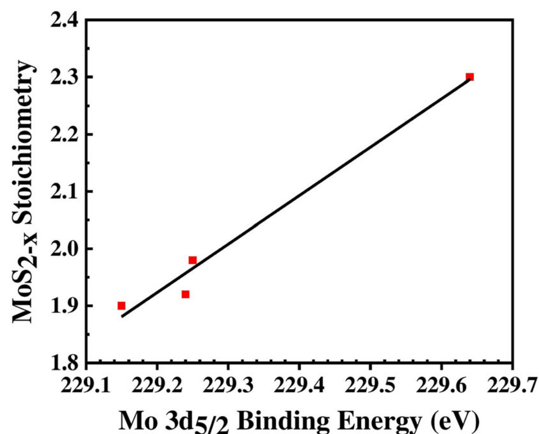

Fig. 7. The plot of the linear relationship between the MoS_{2-x} stoichiometry and Mo $3d_{5/2}$ binding energy.

substrate and MoS_2 film and may result in the formation of the micro-domes in the film. Therefore, it may be thought that the micro-domes become prominent depending on the film thickness. Consequently, the sample Sa2 has hills and valleys on its surface due to these micro domes as seen in both AFM and SEM analysis and the R_{rms} value obtained from AFM analysis for the sample Sa2 was significantly higher due to these micro-domes than the other samples. When it comes to the films grown on SiO_2/Si substrates, as seen from AFM images, such micro-domes did not form on the surfaces of the films due to the smaller coefficient of thermal expansion mismatch between SiO_2/Si substrate and MoS_2 film. The surface morphologies of the films were also evaluated in terms of other surface roughness parameters average roughness (R_a), surface skewness (R_{sk}), and surface kurtosis (R_{ku}). As it is known, the R_a parameter is less sensitive to large deviations from the mean line than the R_{rms} parameter and it can be considered as a general description of the height variations on the surfaces. It was seen that the R_a values were smaller than the R_{rms} values but exhibited similar decrease or increase trends as R_{rms} values. Another roughness parameter R_{sk} describes the symmetry/asymmetry of the distribution of the surface heights about the mean line.

The sample Si1 exhibited a negative R_{sk} value of -0.82 which means the valleys are more predominant than peaks on the surface. Conversely, the samples Si2, Sa1, and Sa2 showed positive skewness values of 3.41, 2.61, and 1.46, respectively. The other roughness parameter is the R_{ku} which describes the level of the flatness or peakedness of the distribution above and below the mean line. R_{ku} values were determined to be less than 3 for sample Si1 and more than 3 for the other samples. This can be considered an indication that the surface of sample Si1 was bumpy and had platykurtic distributions, and the surfaces of the other samples were spiky and had leptokurtic distributions.

Figure 9 shows the histograms of the grain size distributions obtained by AFM analysis in the films. It was seen that the grain size distributions in the films were accumulated at around the submicron-sized grains for the samples.

The average grain size was found to be 0.55 μm, 0.27 μm, 0.23 μm, and 0.20 μm for the samples Si1, Si2, Sa1, and Sa2, respectively.

Figure 10 shows the SEM surface and cross-section images of the MoS_2 films. The surface images of the films exhibited that the films had a smooth and well-packed crystal structure with submicron-sized grains and without any cracks or voids.

No micro-defects such as pinholes were observed on the surface of the films. On the other hand, it was observed that the nanometer-sized grains grown in lateral were uniformly distributed over the surface of the films. The compact microstructure of the films can be also seen from the cross-section SEM images. The formation of highly compact MoS_2 films can be attributed to the grain growth in lateral. The thicknesses of the films were 157 nm, 224 nm, 173 nm, and 212 nm for the samples Si1, Si2, Sa1, and Sa2, according to the cross-section SEM images, respectively. In addition, as seen in Fig. 10d, randomly distributed flower-like micro-domes were observed on the surface of the film for sample Sa2. In order to see the distribution of these micro-domes on the surfaces better, the SEM images of sample Sa2 with lower magnifications are given in Fig. 11. Similar micro-domes on the MoS_2 films were reported by Abouelkhair and et al..[47] The formation of these micro-domes was attributed to the coefficient of thermal expansion mismatch between the sapphire substrate and the MoS_2 film.[45,46] Because of the large surface area of these micro-domes, these kinds of films may be considered remarkable in terms of sensor applications. The increase in the thickness values of the films may have caused the formation of these micro-domes in the films.

SIMS depth profiling was performed to clarify the distributions of the Mo and S elements throughout the film thickness direction. Figure 12 presents the SIMS depth profiles of the MoS_2 films. All samples exhibited very uniform distributions of the constituent elements of Mo and S within the whole thickness of the films. In addition, the profiles of Mo and S elements had almost identical trends for all

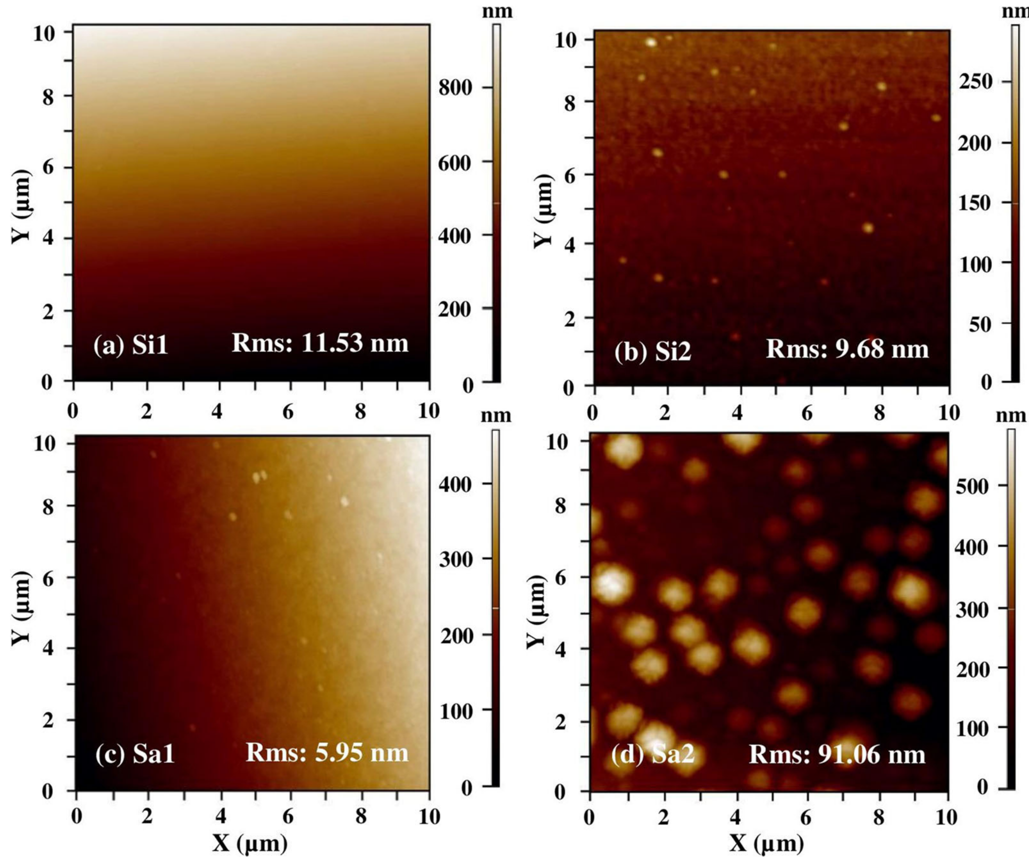

Fig. 8. 2D AFM images of the samples (a) Si1, (b) Si2, (c) Sa1, and (d) Sa2 (scan size: 10 μm × 10 μm).

Table III. Roughness parameters and average grain size values of the films obtained by AFM analysis

	Roughness parameters				
Sample	**Roughness average R_a, nm**	**Root mean square R_{rms}, nm**	**Skewness R_{sk}**	**Kurtosis R_{ku}**	**d, μm**
Si1	9.64	11.53	− 0.82	2.78	0.55
Si2	6.26	9.68	3.41	30.83	0.27
Sa1	4.14	5.95	2.61	28.11	0.23
Sa2	71.14	91.06	1.46	4.39	0.20

the samples. On the other hand, it was observed that the levels of the Si and Al elements which come from the SiO_2/Si and sapphire substrates increased in the region near to the substrates. In the SIMS depth profiles, the converted thickness values using the etching rate were matched well with the thickness values observed in the SEM images.

Transmittance spectra and the plots of absorption coefficient (α) and $(\alpha h\nu)^2$ vs. photon energy ($h\nu$) of the MoS_2 films grown on sapphire substrates were given in Fig. 13. It was observed that the films had average optical transmittance values up to 40% and 44% within the wavelength of 700-1100 nm for the Sa1 and Sa2 samples, respectively, while they had no transmittance down to 500 nm (Fig. 13a).

It is worthy to note that the MoS_2 films are transmissive in the NIR region up to the wavelength of 1100 nm in terms of their possible electro-optical applications in this region. In addition, the films showed clear electronic transitions at around 621 nm (2.01 eV) and 678 nm (1.86 eV); 624 nm (2.0 eV), and 674 nm (1.84 eV) for the samples Sa1 and S2a, respectively. These transitions denoted as A and B in Fig. 13a were attributed to the excitonic transitions at the K point of the Brillouin zone in bulk MoS_2 which are the direct-gap transitions between the maxima of split valance bands and the minimum of the conduction band.[1,29,48,49] Figure 13b and c depicts the plots of the α and $(\alpha h\nu)^{1/2}$ vs. $h\nu$ of the films.

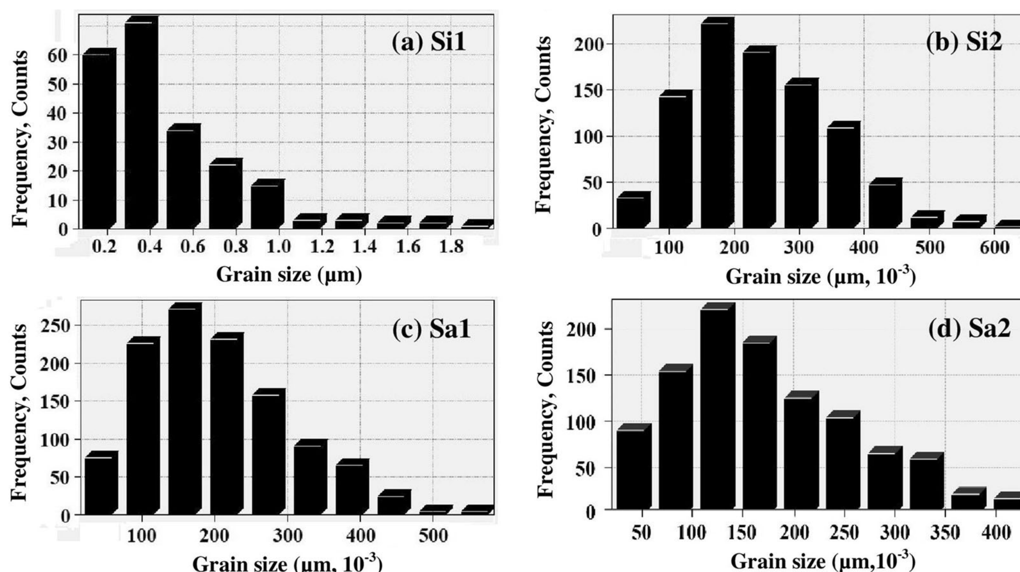

Fig. 9. The histograms of the grain size distributions in the films obtained by AFM analysis for the samples (a) Si1, (b) Si2, (c) Sa1, and (d) Sa2.

The absorption coefficients of the films were calculated using the following relation:

$$\alpha = (1/t)\ln((1/T) \quad (1)$$

where t and T are the thickness and the transmittance of the films, respectively. Absorption coefficients of the films were found to be over 10^5 cm^{-1} in the energy region above 2.5 eV. However, there is an obvious decrease in the value of the absorption coefficient below 2 eV due to the excitonic transitions and band gap transition.

The optical band gaps of the films were calculated by the Tauc method:

$$(\alpha h v)^{1/n} = A(hv - E_g) \quad (2)$$

where h is the Planck constant, v is photon frequency, A is a constant and Eg is the band gap. n equals 2 for indirect allowed transitions. The optical band gaps of the films were estimated as 1.44 eV and 1.56 eV by extrapolating of the linear part to the energy axis of the plot of the $(\alpha h\nu)^{1/2}$ vs. hν for the samples Sa1 and Sa2, respectively. It was seen that the band gap values of the MoS_2 films were larger than that of bulk MoS_2.

FTIR spectroscopy was also used to determine the optical properties of the films in NIR and MIR spectral regions at room temperature. Figure 14a presents the FTIR transmittance spectra of the samples Sa1 and Sa2 in the range of 350–7500 cm^{-1}.

The spectra were also given in the range of 1200–1700 cm^{-1} to be clearly seen the absorptions of the films in Fig. 14b. The grown films exhibited an average transparency of 60% in the range of 1600 cm^{-1} to 7500 cm^{-1} because the sapphire substrate has opacity at wavenumbers below 1600 cm^{-1}. The absorption at 1427 cm^{-1} was attributed to the Mo-S vibration of MoS_2.[50] To evaluate the optical response in NIR and MIR regions of the MoS_2 films grown on SiO_2/Si substrates, FTIR transmittance spectra data in the range of 350–7500 cm^{-1} and FTIR reflectance and absorbance spectra data in the range of 350–4500 cm^{-1} were also collected and given in Fig. 15.

The observed absorption peak at around 467 cm^{-1} in the expanded transmittance spectra of the films was attributed to the Mo-S vibration of MoS_2 (Fig. 15b).[51] The strong absorptions located at 614 cm^{-1} and 1103 cm^{-1} were attributed to Si-Si stretch vibration of the Si substrate and Si-O stretch vibration originating from interstitial O impurities, respectively.[52] On the other hand, it was seen that the MoS_2 films grown on SiO_2/Si had a strong broadband absorption in the range of 850–2850 cm^{-1} (3.5–11.8 μm) (Fig. 15c). Similar broadband absorption in the NIR and MIR regions was obtained by Goswami and et al. for the bulk MoS_2 films.[24] As expected, the absorption of the films increased with the film thickness. Owing to this strong absorption of the films in these regions, it is considered that they can be used for IR detection applications.[53] The films showed an average IR reflection of 87% in the range of 350–7000 cm^{-1} (27.7–1.5 μm). Therefore, the films can be used as IR shielding coating for several applications in this spectral region due to their high reflectance properties. Moreover, in the reflectance and absorbance spectra of the films, vibrational peaks centered at around 467 cm^{-1}, 611/614 cm^{-1}, and 1091/1093 cm^{-1} were attributed to the Mo-S vibration, Si-Si stretch vibration of Si substrate, and Si-O-Si stretch vibration originating from SiO_2/Si substrates, respectively.

To investigate the electrical transport properties of the MoS_2 thin films, Hall effect measurements

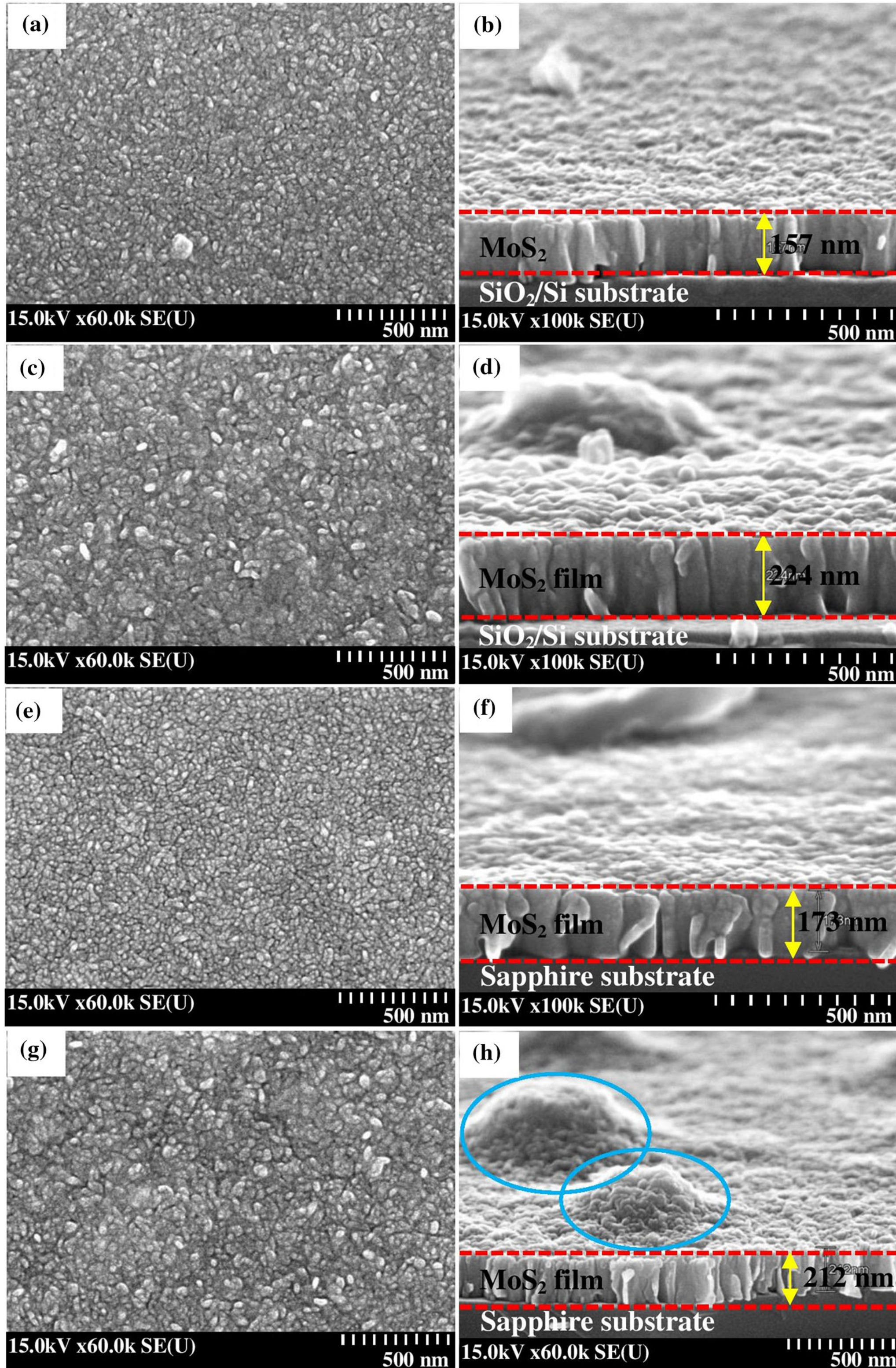

Fig. 10. SEM surface and cross-section images of MoS_2 films for the samples (a,b) Si1, (c,d) Si2, (e,f) Sa1, and (g,h) Sa2, respectively.

were conducted at room temperature at B = 0.4 T and the resistivity, carrier concentration, Hall mobility, and Hall coefficient were calculated by the Van der Pauw method. Calculated electrical parameters were listed in Table IV.

The films showed both n-type and p-type conductivity. This electrical transport behavior of the films

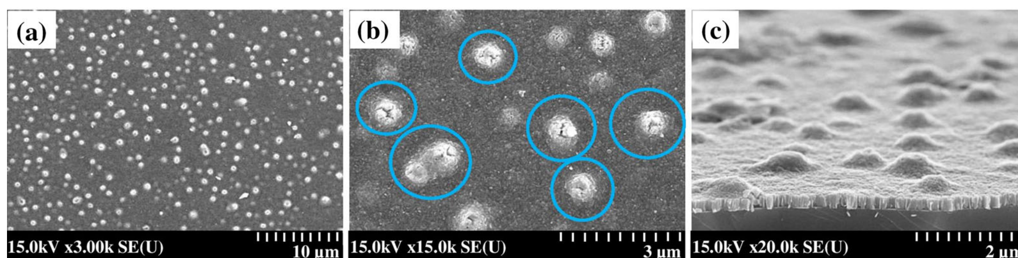

Fig. 11. SEM surface images of the sample Sa2 for (a) 3 k magnification, (b) 15 k magnification, and the cross-section image of the sample Sa2 for (c) 20 k magnification.

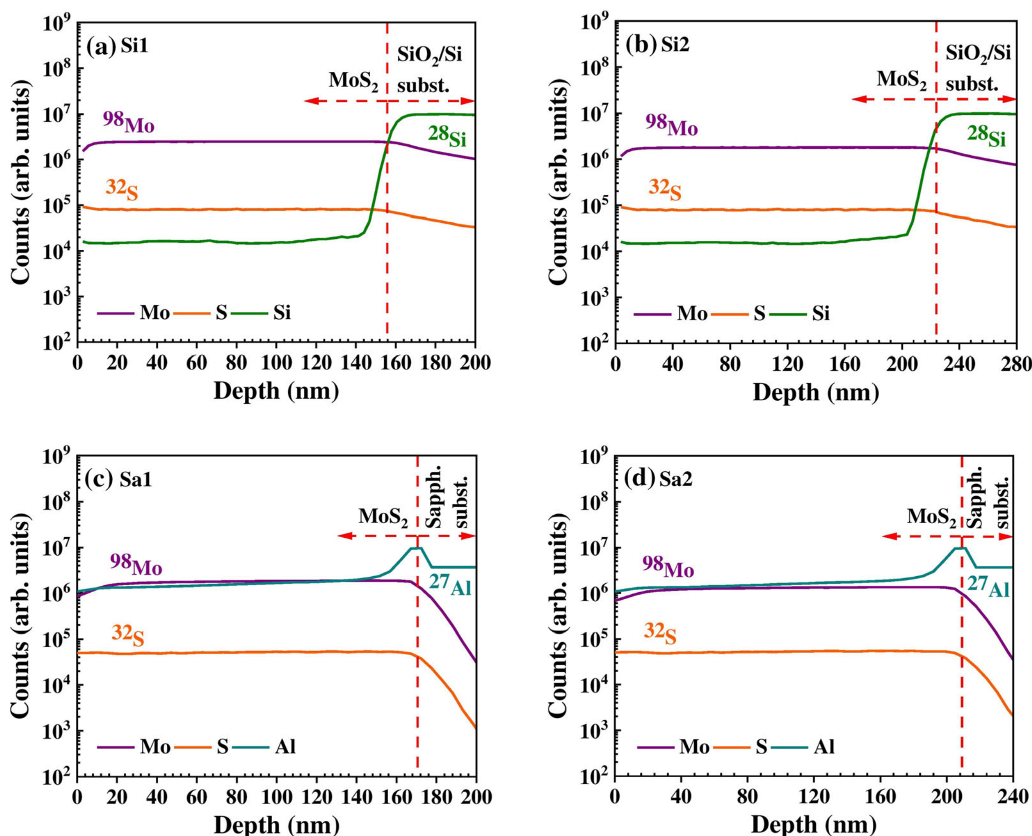

Fig. 12. SIMS depth profiles of the samples (a) Si1, (b) Si2, (c) Sa1, and (d) Sa2.

was attributed to the strong spin–orbit coupling caused by transition metal (Mo) d orbitals in MoS_2.[54,55] The formation of the oxygen impurities behaving like acceptors in the films during the sulfurization process might be another reason for the transformation of the n-type conductivity to p-type. The carrier concentrations of the films prepared on sapphire substrates were higher than those of the films prepared on SiO_2/Si substrates. However, the lower mobility values were obtained for the films prepared on sapphire substrates. In addition, it was seen that the mobility values of the films obtained in this study were higher than those of the films produced by two-zoned CVD in our previous study.[39]

CONCLUSION

In summary, the MoS_2 films with different thicknesses were prepared by sulfurization of Mo precursor films deposited by DC magnetron sputtering on SiO_2/Si and c-plane sapphire substrates. The sulfurization process was carried out in a single-zoned CVD furnace with sulfur powder at 900°C. After sulfurization, the structural, morphological, optical, and electrical properties of the films were analyzed in detail. The appearance of a (002) diffraction peak in the XRD patterns of samples Sa1 and Sa2 showed that the films grown on sapphire substrates exhibited better crystallization and a well-stacked layered structure than the films on SiO_2/Si substrates. The formation of the

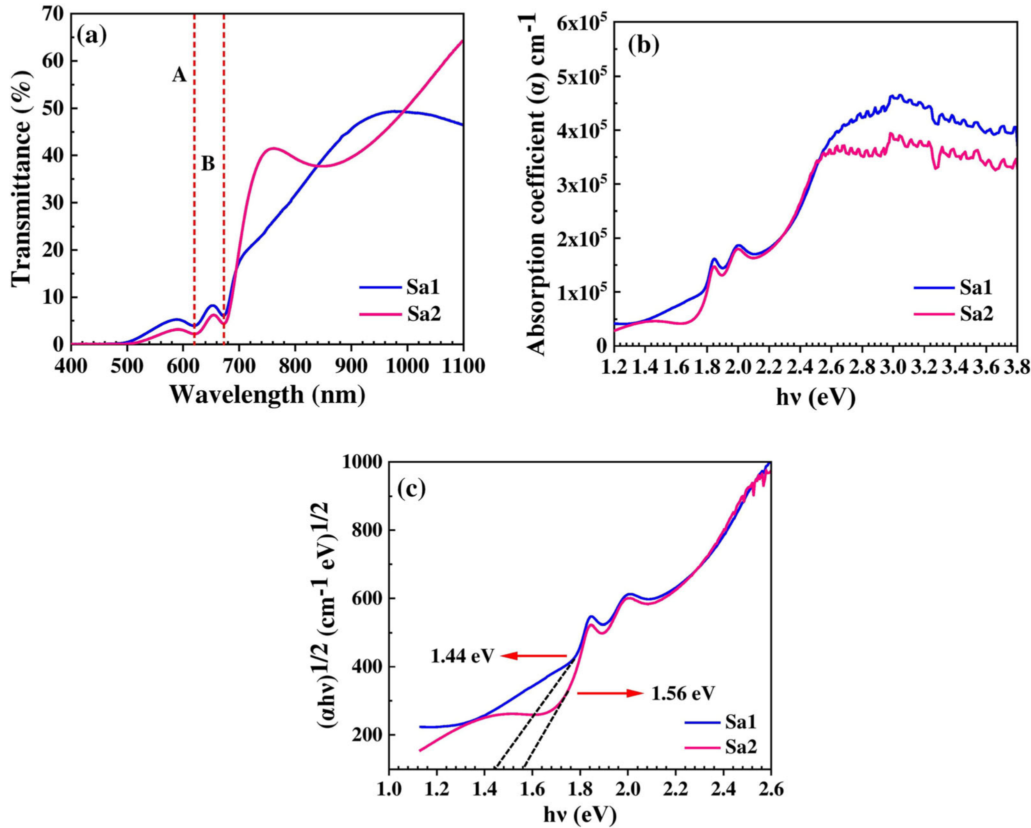

Fig. 13. (a) Transmittance spectra and the plots of (b) α and (c) $(\alpha h\nu)^{1/2}$ versus hν of the samples Sa1 and Sa2.

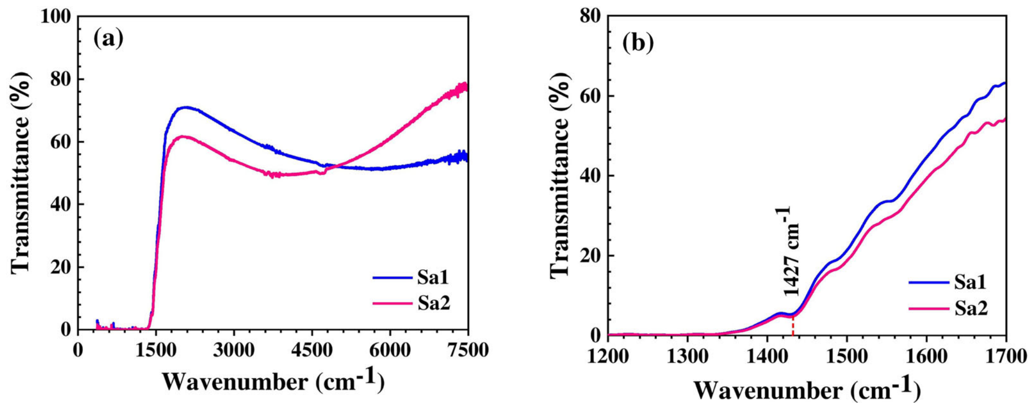

Fig. 14. FTIR transmittance spectra of the samples Sa1 and Sa2 in the (a) 350–7500 cm^{-1} and (b) 1200–1700 cm^{-1} wavenumber range

hexagonal phase of bulk MoS_2 was also confirmed by the characteristic modes E^1_{2g} and A_{1g} with a frequency difference of $\sim$ 26 cm^{-1} via Raman spectroscopy analysis. EDX analysis showed that the compositions of the films were near-stoichiometric. However, a small shift was observed to the lower binding energies in the Mo $3d_{5/2}$ peak positions due to the valency of Mo below +4 depending on the compositional ratios of the films in XPS spectra. From the AFM and SEM analysis, it was seen that the films had uniform surfaces and a well-packed crystal structure. However, the strain due to thermal expansion coefficient mismatch between the sapphire substrate and MoS_2 film resulted in the formation of the micro-domes on the surface of the film for the sample Sa2. This was associated with larger film thickness of the sample Sa2 than the sample Sa1. Since the formation of such micro-domes was not observed in the films grown on SiO_2/Si substrates, it has been concluded that the strain in the films grown on sapphire substrates is of great importance on the morphological properties of the films and should be certainly taken into consideration in the process of the MoS_2 films grown by this method. Because of the high absorption and

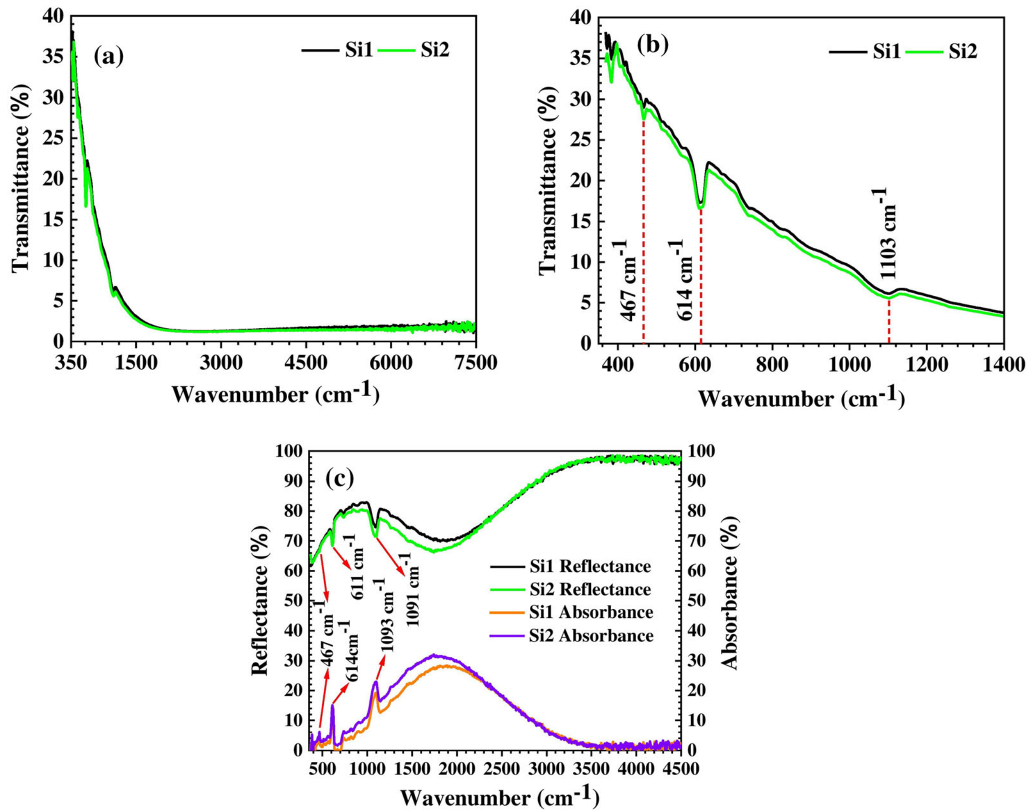

Fig. 15. (a) FTIR transmittance, (b) expanded FTIR transmittance and (c) reflectance and absorbance spectra of the samples Si1 and Si2.

Table IV. Electrical parameters of the grown MoS_2 films

Sample	Resistivity (Ohm cm)	Carrier Concentration (1/cm^3)	Mobility (cm^2/V s)	Conductivity type
Si1	3.35E + 02	7.03E + 13	2.65E + 02	n-type
Si2	1.10E + 02	1.04E + 14	5.51E + 02	p-type
Sa1	6.97E + 02	1.96E + 15	4.67E + 00	n-type
Sa2	8.28E + 02	3.16E + 15	2.40E + 00	p-type

reflection properties of the films grown on SiO_2/Si and sapphire substrates in the NIR and MIR regions, it was suggested that they can be used for NIR and MIR photodetectors and also for IR shielding coating applications. Additionally, it can be concluded that the decrease in the volume of the sulfurization atmosphere and thus the increase in the chalcogen vapor pressure strongly influenced the compositions of the films and brought them closer to an ideal value of 2 and increased the mobility values of the films. Moreover, the formation of the micro-domes on the surfaces of the films grown on sapphire substrate with an increase in the film thicknesses in this study was another difference and therefore the films may be considered remarkable in terms of sensor applications.

ACKNOWLEDGMENTS

This work is supported by the Presidency of Turkey, Presidency of Strategy and Budget, and TUBITAK under the 2016K121220 and 115F280 project numbers, respectively, and by the Belarusian State Programme for Research « Physical material science, new materials and technologies » .

CONFLICT OF INTEREST

The authors declare that they have no known competing financial interests or personal relationships that could have appeared to influence the work reported in this paper.

REFERENCES

1. C. Ahn, J. Lee, H.U. Kim, H. Bark, M. Jeon, G.H. Ryu, Z. Lee, G.Y. Yeom, K. Kim, J. Jung, Y. Kim, C. Lee, and T. Kim, *Adv. Mater.* 27, 5223 (2015).
2. S. Park, N. Mutz, T. Schultz, S. Blumstengel, A. Han, A. Aljarb, L.J. Li, E.J.W. List-Kratochvil, P. Amsalem, and N. Koch, *2D Mater* 5, 025003 (2018).
3. A.L. Tan, H.A. Hassan, and S.S. Ng, *J. Mater. Sci.: Mater. Electron.* 30, 10419 (2019).

4. Y. Wang, L.T. Tseng, P.P. Murmu, N. Bao, J. Kennedy, M. Ionesc, J. Ding, K. Suzuki, S. Li, and J. Yi, *Mater. Des.* 121, 77 (2017).
5. S. Ahmed, X. Ding, N. Bao, P. Bian, R. Zheng, Y. Wang, P.P. Murmu, J.V. Kennedy, R. Liu, H. Fan, K. Suzuki, J. Ding, and J. Yi, *Chem. Mater.* 29, 9066 (2017).
6. X. Zhang, H. Nan, S. Xiao, X. Wan, Z. Ni, X. Gu, and K. Ostrikov, *Acs. Appl. Mater. Inter.* 9, 42121 (2017).
7. A. Antonelou, G. Syrrokostas, L. Sygellou, G. Leftheriotis, V. Dracopoulos, and S.N. Yannopoulos, *Nanotechnology* 27, 045404 (2016).
8. S.Z. Butler, S.M. Hollen, L. Cao, Y. Cui, J.A. Gupta, H.R. Gutiérrez, T.F. Heinz, S.S. Hong, J. Huang, A.F. Ismach, E. Johnston-Halperin, M. Kuno, V.V. Plashnitsa, R.D. Robinson, R.S. Ruoff, S. Salahuddin, J. Shan, L. Shi, M.G. Spencer, M. Terrones, W. Windl, and J.E. Goldberger, *ACS Nano* 7, 2898 (2013).
9. J.J. Pyeon, S.H. Kim, D.S. Jeong, S.H. Baek, C.Y. Kang, J.S. Kim, and S.K. Kim, *Nanoscale* 8, 10792 (2016).
10. J. Park, N. Choudhary, J. Smith, G. Lee, M. Kim, and W. Choi, *Appl. Phys. Lett.* 106, 012104 (2015).
11. H. Kwon, S. Baik, J.E. Jang, J. Jang, S. Kim, C.P. Grigoropoulos, and H.J. Kwon, *Electronics* 8, 222 (2019).
12. H. Zeng, G.B. Liu, J. Dai, Y. Yan, B. Zhu, R. He, L. Xie, S. Xu, X. Chen, W. Yao, and X. Cui, *Sci. Rep.* 3, 1608 (2013).
13. R. Xie, Y. Li, H. Huang, H. Hu, T. Li, B. Guo, L. Su, X. Zhang, G. Xu, L. Wang, F. Chi, H. Liu, and Y. Ma, *Ceram. Int.* 45, 18501 (2019).
14. G. Pradhan and A.K. Sharma, *Appl. Surf. Sci.* 479, 1236 (2019).
15. K.F. Mak, C. Lee, J. Hone, J. Shan, and T.F. Heinz, *Phys. Rev. Lett.* 105, 136805 (2010).
16. S.S. Ding, W.Q. Huang, Y.C. Yang, B.X. Zhou, W.Y. Hu, M.Q. Long, P. Peng, and G.F. Huang, *J. Appl. Phys.* 119, 205704 (2016).
17. O. Lopez-Sanchez, D. Lembke, M. Kayci, A. Radenovic, and A. Kis, *Nat. Nanotechnol.* 8, 497 (2013).
18. X. Gan, H. Zhao, and X. Quan, *Biosens. Bioelectron.* 89, 56 (2017).
19. D.J. Late, Y.K. Huang, B. Liu, J. Acharya, S.N. Shirodkar, J. Luo, A. Yan, D. Charles, U.V. Waghmare, V.P. Dravid, and C.N. Rao, *ACS Nano* 7, 4879 (2013).
20. W. Choi, M.Y. Cho, A. Konar, J.H. Lee, G.B. Cha, S.C. Hong, S. Kim, J. Kim, D. Jena, J. Joo, and S. Kim, *Adv. Mater.* 24, 5832 (2012).
21. Z. Yang, X. Liu, X. Zou, J. Wang, C. Ma, C. Jiang, J.C. Ho, C. Pan, X. Xiao, J. Xiong, and L. Liao, *Adv. Funct. Mater.* 27, 1602250 (2016).
22. H. Xu, L. Xin, L. Liu, D. Pang, Y. Jiao, R. Cong, and W. Yu, *Mater. Lett.* 238, 13 (2019).
23. R.D. Nikam, P.A. Sonawane, R. Sankar, and Y.T. Chen, *Nano Energy* 32, 454 (2017).
24. A. Goswami, P. Dhandaria, S. Pal, R. McGee, F. Khan, Ž. Antić, R. Gaikwad, K. Prashanthi, and T. Thundat, *Nano Res.* 10, 3571 (2017).
25. G. Eda, H. Yamaguchi, D. Voiry, T. Fujita, M. Chen, and M. Chhowalla, *Nano Lett.* 11, 5111 (2011).
26. P. Yiya, M. Zhaoyu, Z. Chang, L. Jun, Y. Weichao, J. YunBo, and Q. Yitai, *Chem. Lett.* 30, 772 (2001).
27. C. Muratore, J.J. Hu, B. Wang, M.A. Haque, J.E. Bultman, M.L. Jespersen, P.J. Shamberger, M.E. McConney, R.D. Naguy, and A.A. Voevodin, *Appl. Phys. Lett.* 104, 261604 (2014).
28. Y.H. Lee, X.Q. Zhang, W. Zhang, M.T. Chang, C.T. Lin, K.D. Chang, Y.C. Yu, J.T. Wang, C.S. Chang, L.J. Li, and T.W. Lin, *Adv. Mater.* 24, 2320 (2012).
29. S. Deb, P. Chakrabarti, P.K. Mohapatra, B.K. Barick, and S. Dhar, *Appl. Surf. Sci.* 445, 542 (2018).
30. F. Chen, W. Su, S. Ding, and L. Fu, *Ceram. Int.* 45, 15091 (2019).
31. A. Splendiani, L. Sun, Y. Zhang, T. Li, J. Kim, C.Y. Chim, G. Galli, and F. Wang, *Nano Lett.* 10, 1271 (2010).
32. B. Radisavljevic, A. Radenovic, J. Brivio, V. Giacometti, and A. Kis, *Nat. Nanotechnol.* 6, 147 (2011).
33. S. Wang, M. Pacios, H. Bhaskaran, and J.H. Warner, *Nanotechnology* 27, 085604 (2016).
34. Y.F. Lim, K. Priyadarshi, F. Bussolotti, P.K. Gogoi, X. Cui, M. Yang, J. Pan, S.W. Tong, S. Wang, S.J. Pennycook, K.E.J. Goh, A.T.S. Wee, S.L. Wong, and D. Chi, *ACS Nano* 12, 1339 (2018).
35. K. Lee, R. Gatensby, N. McEvoy, T. Hallam, and G.S. Duesberg, *Adv. Mater.* 25, 6699 (2013).
36. K.M. McCreary, A.T. Hanbicki, J.T. Robinson, E. Cobas, J.C. Culbertson, A.L. Friedman, G.G. Jernigan, and B.T. Jonker, *Adv. Funct. Mater.* 24, 6449 (2014).
37. K.K. Liu, W. Zhang, Y.H. Lee, Y.C. Lin, M.T. Chang, C.Y. Su, C.S. Chang, H. Li, Y. Shi, H. Zhang, C.S. Lai, and L.J. Li, *Nano Lett.* 12, 1538 (2012).
38. K. Kang, S. Xie, L. Huang, Y. Han, P.Y. Huang, K.F. Mak, C.J. Kim, D. Muller, and J. Park, *Nature* 520, 656 (2015).
39. S. Ozcelik, N. Akcay, and M. Tivanov, *Int. J. Nanosci.* 18, 1940037 (2019).
40. H. Terrones, E. Del Corro, S. Feng, J.M. Poumirol, D. Rhodes, D. Smirnov, N.R. Pradhan, Z. Lin, M.A.T. Nguyen, A.L. Elias, T.E. Mallouk, L. Balicas, M.A. Pimenta, and M. Terrones, *Sci. Rep.* 4, 4215 (2014).
41. X. Zhang, W.P. Han, J.B. Wu, S. Milana, Y. Lu, Q.Q. Li, A.C. Ferrari, and P.H. Tan, *Phys. Rev. B* 87, 115413 (2013).
42. R.A. Evarestov and A.V. Bandura, *J. Comput. Chem.* 39, 2163 (2018).
43. C. Zeng, J. Pu, H. Wang, S. Zheng, L. Wang, and Q. Xue, *Ceram. Int.* 45, 15834 (2019).
44. M.A. Baker, R. Gilmore, C. Lenardi, and W. Gissler, *Appl. Surf. Sci.* 150, 255 (1999).
45. W.M. Yim and R.J. Paff, *J. Appl. Phys.* 45, 1456 (1974).
46. E.M. Dudnik and V.K. Oganesyan, *Sov. Powder Metall. Met. Ceram.* 5, 125 (1966).
47. H.M. Abouelkhair, N.A. Orlovskaya, and R.E. Peale, *IEEE 4th PVSC*, 2324 (2017).
48. Q.H. Wang, K. Kalantar-Zadeh, A. Kis, J.N. Coleman, and M.S. Strano, *Nat. Nanotechnol.* 7, 699 (2012).
49. N.B. Shinde, B. Francis, M.S. Ramachandra Rao, B.D. Ryu, S. Chandramohan, and S.K. Eswaran, *APL Mater.* 7, 081113 (2019).
50. W. Feng, L. Chen, M. Qin, X. Zhou, Q. Zhang, Y. Miao, K. Qiu, Y. Zhang, and C. He, *Sci. Rep.* 5, 17422 (2015).
51. M. Yi and C. Zhang, *Rsc Adv.* 8, 9564 (2018).
52. Z.D. Sha, Y. Yan, W.X. Qin, X.M. Wu, and J. Zhuge, *J. Phys. D Appl. Phys.* 39, 3240 (2006).
53. X. Wang, P. Wang, J. Wang, W. Hu, X. Zhou, N. Guo, H. Huang, S. Sun, H. Shen, T. Lin, M. Tang, L. Liao, A. Jiang, J. Sun, X. Meng, X. Chen, W. Lu, and J. Chu, *Adv. Mater.* 27, 6575 (2015).
54. M. Qi, J. Xiao, and C. Gong, *Semicond. Sci. Tech.* 34, 045017 (2019).
55. Q. Chen, L.L. Li, and F.M. Peeters, *Phys. Rev.* 97, 085437 (2018).

Publisher's Note Springer Nature remains neutral with regard to jurisdictional claims in published maps and institutional affiliations.